A binding site outside the canonical PDZ domain determines the specific interaction between Shank and SAPAP and their function

Menglong Zeng[a,1], Yuan Shang[a,1], Tingfeng Guo[a], Qinghai He[a], Wing-Ho Yung[b], Kai Liu[a,c], and Mingjie Zhang[a,c,2]

[a]Division of Life Science, State Key Laboratory of Molecular Neuroscience, Hong Kong University of Science and Technology, Hong Kong, China; [b]School of Biomedical Sciences, Faculty of Medicine, The Chinese University of Hong Kong, Hong Kong, China; and [c]Center of Systems Biology and Human Health, School of Science and Institute for Advanced Study, Hong Kong University of Science and Technology, Hong Kong, China

Shank and SAPAP (synapse-associated protein 90/postsynaptic density-95–associated protein) are two highly abundant scaffold proteins that directly interact with each other to regulate excitatory synapse development and plasticity. Mutations of *SAPAP*, but not other reported Shank PDZ domain binders, share a significant overlap on behavioral abnormalities with the mutations of *Shank* both in patients and in animal models. The molecular mechanism governing the exquisite specificity of the Shank/SAPAP interaction is not clear, however. Here we report that a sequence preceding the canonical PDZ domain of Shank, together with the elongated PDZ BC loop, form another binding site for a sequence upstream of the SAPAP PDZ-binding motif, leading to a several hundred-fold increase in the affinity of the Shank/SAPAP interaction. We provide evidence that the specific interaction afforded by this newly identified site is required for Shank synaptic targeting and the Shank-induced synaptic activity increase. Our study provides a molecular explanation of how Shank and SAPAP dosage changes due to their gene copy number variations can contribute to different psychiatric disorders.

Shank | SAPAP | PDZ | synapse | specific interaction

Postsynaptic density (PSD) at excitatory synapses refers to disk-shaped, densely packed mega-protein assemblies located beneath postsynaptic membranes (1–5). A set of highly abundant scaffold proteins, including DLGs (disc large proteins including PSD-95, PSD-93, and SAP102), SAPAP (synapse-associated protein 90/postsynaptic density-95–associated protein; also known as GKAP or DLGAP), and Shank, are known to be critical for the formation, stability, and neuronal activity-dependent dynamic regulations of PSDs (6–17). In addition to orchestrating PSD formation, these scaffold proteins also serve to control the trafficking and clustering of receptors on the plasma membranes and to interface with actin cytoskeletons at synapses (15, 18, 19). Mutations of DLGs, SAPAP, and Shank have been found to cause or associate with various psychiatric disorders, including autism spectrum disorder (ASD), depression, and schizophrenia (20–28), further supporting the importance of these proteins in normal brain development and functions.

Electron and superresolution light microscopy imaging studies (4, 5, 18, 29–32) have revealed that proteins in PSDs form distinct layers along the axodendritic axis of synapses with a sequential order of membrane-spanning glutamate receptors and cell adhesion molecules, DLGs, the SAPAP and Shank scaffolds, and actin cytoskeletons. Such a distinct layered structure in PSDs depends critically on the specific interactions between the scaffold proteins. For example, the phosphorylation-dependent interaction between DLG GK domain and the N-terminal repeating sequences of SAPAP positions SAPAP beneath DLGs (33), and the interaction between the SAPAP PDZ-binding motif (PBM) and Shank PDZ domain functions to place Shank at a deeper layer in PSD (7).

The critical roles of the PSD scaffold proteins in normal brain physiology and human psychiatric disorders caused by mutations of genes encoding these proteins have spurred great interest in studying the underlying molecular mechanisms governing these proteins under both physiological and disease conditions. One popular approach to this is to identify proteins that can interact with these scaffolds by various screening approaches, such as yeast two-hybrid screenings, phage displays, proteomics, and, more recently, large-scale genomic-based approaches. These screens have identified a huge list of proteins that have the potential to interact with the PSD scaffolds like DLGs, SAPAP, and Shank. For example, several dozens of proteins other than glutamate receptors and neuronal adhesion molecules have been reported to bind to the PDZ domains of PSD-95, and approximately a dozen proteins other than SAPAP have been shown to use their PBMs (PDZ binding motifs) to bind to the Shank PDZ domain.

Although identification of these scaffold binding proteins certainly has enriched our knowledge of the potential protein networks operating in synapses, a concomitant problem is that such still-growing protein–protein interaction networks are extraordinary complicated and extremely difficult to interpret. A problematic issue, as we articulate below, is that many of such interactions reported in the past might not be physiologically irrelevant. We also believe that similar problems are widespread in systems other than neuronal synapses, given that scaffold protein-mediated signal transductions is a common strategy used by essentially all tissue types in living kingdoms.

Significance

Synaptic scaffold proteins, such as Shank and SAPAP, play critical roles in organizing protein complexes essential for neuronal development and signaling. Approximately 50% of protein concentration changes resulting from genetic mutations can cause various forms of psychiatric disorders; however, the molecular mechanism underlying such dosage-sensitive functional changes for the two scaffold proteins are not clear. Here we discover that a previously unrecognized PDZ domain-mediated binding mode renders an exquisitely specific interaction between Shank and SAPAP. Mutations of either of these proteins lead to quantitative reductions of the Shank/SAPAP complex in synapses. We also demonstrate that a Shank/SAPAP complex inhibitory peptide can modulate excitatory synaptic activities, providing a proof of concept of modulating synaptic activities by targeting the Shank PDZ domain.

BIOCHEMISTRY

In view of the critical roles of SAPAP and Shank in synaptic development and plasticity, it is conceptually not difficult to rationalize that the loss-of-function mutations of *SAPAP* and *Shank* caused by total deletions or effective null mutations can lead to ASD-like phenotypes in model organisms, presumably due to total elimination of the protein interaction network concerning these two proteins and consequent impairment of synaptic development and plasticity (34–41). Essentially all *SAPAP* and *Shank* mutations found in patients with ASD or other psychiatric disorders are heterozygous in nature, however (28, 42–45). In theory, under the majority of these mutation conditions, a mere 50% decrease caused by a deletion/null mutation or a 50% increase due to gene duplications of *SAPAP* or *Shank* can cause disease, indicating that the physiological functions of the human nervous system are highly sensitive to the dosages of these two proteins, and many other proteins encoded by psychiatric disorder genes as well (20, 46). Opposite to reduced synaptogenesis and decreased excitatory synaptic strengths in *Shank* deletion mice (34–36), a ~50% protein increase of Shank3 in mice can lead to overactivation of excitatory synaptic currents and can cause manic-like phenotypes (47). Furthermore, duplication of *Shank3* has been found in patients suffering from epilepsy and other hyperactivity-related symptoms (47).

Corroborating the above observations, we note that, in addition to scaffold proteins, the functions of another major category of psychiatric disorder genes are directly involved in the regulation of synaptic protein expression or metabolism. For example, FMRP (Fragile X Mental Retardation Protein) is an RNA-binding protein linked to trafficking and translation of synaptic proteins (48), the TSC1/TSC2 complex is known to regulate mTOR-mediated protein translations (49, 50), and Ube3a acts as an E3 ligase to regulate synaptic protein turnover (51). It becomes increasingly obvious, albeit with poorly understood underpinning mechanisms, that mutations of one gene (or one common set of genes) can lead to different psychiatric disorders (52). It is possible that different mutations on one gene (e.g., *Shank3* deletion vs. duplication) can directly lead to opposite changes in the expression level of the encoded protein, thereby leading to opposing neuronal activity changes (53). Alternatively, different mutations may stimulate or suppress the expression/metabolic activities of an encoded gene, and thus indirectly modulate changes in synaptic protein levels and subsequent divergent phenotypic outcomes.

Disparities between specific and dosage-dependent biological functions and reported multiple binding partners, often with unrelated functions, for a given protein are widespread in the literature. This issue is even more acute for scaffold proteins, given that the majority of these proteins do not have catalytic activity and thus generally cannot amplify activity changes by themselves. Taking the Shank and SAPAP interaction for an example, the PDZ domain of Shank has been reported to bind to many proteins other than SAPAP in synapses, including neuroligins (54), β-PIX (55), calcium channels (56, 57), mGluR (15), and α-latrotoxin (58). The reported interactions between Shank and these targets are of comparable and modest affinities with dissociation constants in the range of a few micromols (59). This immediately creates a biochemical dilemma. Because Shank interacts with all of these proteins more or less with equal affinity, a 50% decrease/increase in Shank3 resulting from *Shank3* deletions/duplications would have a minimal impact on the overall Shank3/target complex distribution (e.g., a mere ~5% change for each complex if Shank were evenly distributed among 10 different targets). Correspondingly, obvious functional changes due to an ~50% change in Shank level in human brain would not be expected.

The foregoing dilemma would not exist if one Shank binding partner (e.g., SAPAP) had a much higher binding affinity than the other reported binding partners. Because we demonstrate in this work that SAPAP binds to Shank with an ~100-fold stronger affinity than other reported Shank-binding proteins. Under such a scenario, almost all of Shank in synapses is calculated to be in complex with SAPAP, and changes in Shank or SAPAP dosage would have a major impact on the concentrations of the Shank/SAPAP complex instead of other reported Shank complexes. The unique binding specificity and affinity between Shank and SAPAP is afforded by a previously unrecognized binding site outside the canonical PDZ/target binding pocket. This work emphasizes that quantitative biochemical characterizations of scaffold protein-mediated interactions are critically important in understanding the mechanistic bases governing their functions in broad biological processes such as synaptic functions in this case.

Results

Shank Interacts with SAPAP with an Unexpectedly High Affinity. We first verified the well-accepted PDZ domain-mediated interaction between Shank and SAPAP using purified recombinant protein of Shank3 PDZ (residues 563–665) and a synthetic hexapeptide corresponding to SAPAP3 PBM (EAQTRL; residues 972–977) (Fig. 1A). Isothermal titration calorimetry (ITC)-based assays showed that the SAPAP3 PBM binds to Shank3 PDZ with a K_d of ~5.8 μM (Fig. 1 B and C), a value typical for the majority of the canonical PDZ and PBM interactions (60). However, as we reasoned in the introductory section, such a modest binding affinity between Shank3 PDZ and SAPAP3 PBM is unlikely to be sufficient for the specific functional interactions between Shank3 and SAPAP3 observed in vivo.

We found that each family member of Shank has an SH3 domain closely proceeding the PDZ domain, and that each SAPAP contains a stretch of proline-rich sequence upstream of its PBM (Fig. 1A). Thus, we hypothesized that the Shank SH3-PDZ tandem may interact with a longer version of SAPAP C-terminal tail containing the "Pro-rich" sequence with a higher affinity than the PDZ/PBM interaction alone. Indeed, we discovered that the Shank3 SH3-PDZ tandem (residues 461–665) and an elongated SAPAP3 C terminus (residues 900–977) interact with each other with an affinity ~100-fold stronger than that of the PDZ/PBM interaction (K_d ~0.045 μM vs. ~5.8 μM) (Fig. 1 B and C, C1). This biochemical finding uncovers a previously unrecognized, highly specific interaction between Shank3 and SAPAP3.

Interestingly, we detected no direct interactions between the isolated Shank3 SH3 domain and the elongated SAPAP3-CT (Fig. 1C, C2). In addition, deletions of the SH3 domain from the SH3-PDZ tandem and the Pro-rich sequence from SAPAP3 individually or combined had no detectable impact on the strong interaction between Shank3 and SAPAP3 (Fig. 1C), indicating that the SH3 domain of Shank3 does not contribute to the strong interaction between Shank3 and SAPAP3.

Further fine mapping analysis revealed that an N-terminal extended Shank3 PDZ domain (residues 533–665, denoted "N-PDZ" for the N-terminal extended PDZ domain) and the last 12 residues of SAPAP3 (residues 966–977, referred to as "E-PBM" for the extended PDZ binding motif) are the minimal sequences for the strong interaction between Shank3 and SAPAP3 (Fig. 1C). Our mapping data also indicate that there exists another binding site in addition to the canonical PDZ-PBM binding site in the Shank3 N-PDZ/SAPAP3 E-PBM interaction. This secondary binding site is attributed by the extended sequence of Shank3 N-PDZ (specifically, residues 533–563) and residues upstream of the QTRL motif of SAPAP3 E-PBM (residues 956–973) (Fig. 1A). This conclusion is drawn by the data that deletion of the QTRL motif completely eliminated the binding of SAPAP3 E-PBM to the canonical Shank3 PDZ, but did not totally disrupt its binding to Shank3 SH3-PDZ (Fig. 1C, C3).

Considering that both the N-terminal extension sequence of Shank PDZ and the extended sequence of SAPAP-CT are highly conserved both among their different family members (Shank1-3 or SAPAP1-4) and during the evolution of both proteins (Fig. 1 E and F), we predict that all Shank-SAPAP interactions use the binding mode elucidated here and are of high affinity.
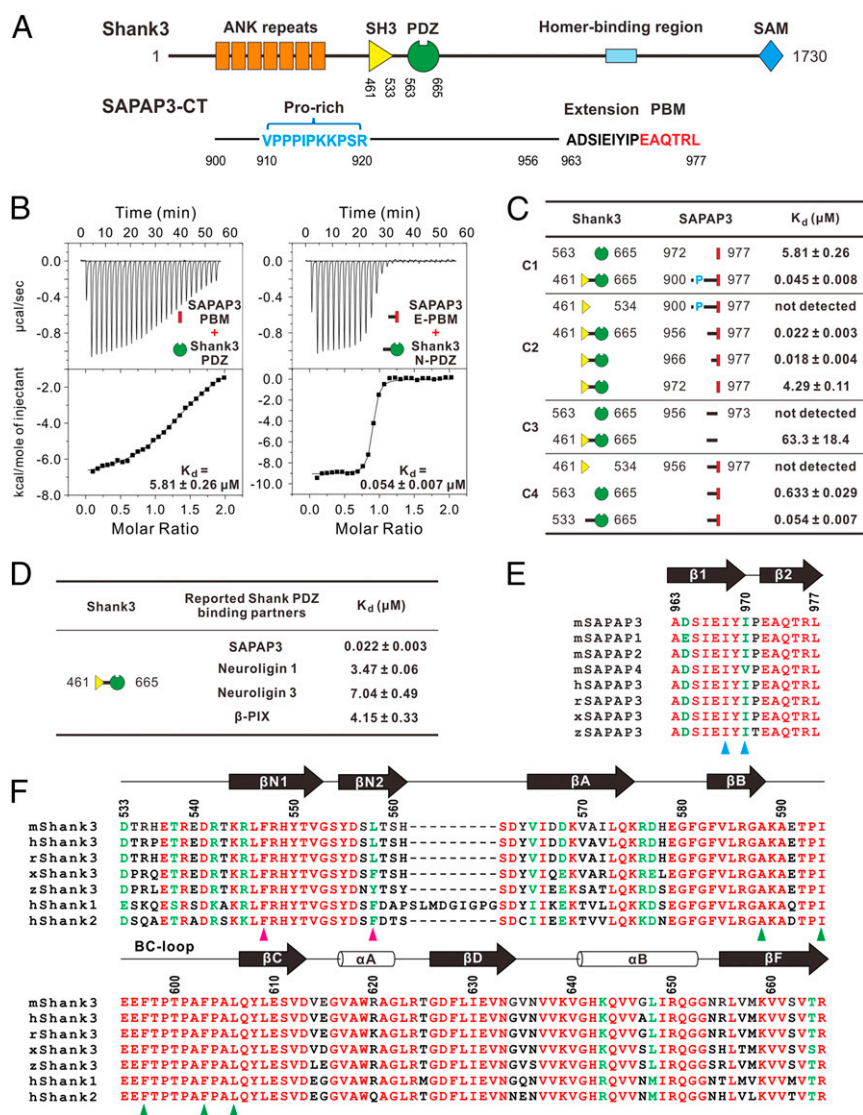
Fig. 1. Shank3 N-PDZ binds to SAPAP3 E-PBM with high affinity and specificity. (*A*) Schematic diagram showing the domain organizations of Shank3 and SAPAP3. (*B*) ITC-based measurements quantifying the binding affinity between the canonical SAPAP3 PBM and Shank3 PDZ (*Left*) and SAPAP3 E-PBM and Shank3 N-PDZ (*Right*). (*C*) ITC-based measurements summarizing the binding affinities of various Shank3 proteins and SAPAP3 C termini. The mapping results show that Shank3 N-PDZ and SAPAP3 E-PBM are the minimal regions for the two proteins to interact with high affinity. (*D*) ITC-based measurements comparing the binding affinities of Shank3 SH3-PDZ and several previously reported Shank PDZ-binding partners. The proteins assayed in each experiment were SAPAP3 E-PBM, the entire cytoplasmic tails of neuroligin 1 or 3, and β-PIX coiled-coil PBM. (*E*) Sequence alignment of the last 15 residues from different SAPAPs. (*F*) Structure-based sequence alignment of the N-terminal extended PDZ domain from different Shank proteins. In these alignments, totally conserved residues are labeled in red, and conserved residues are in green. The hydrophobic residues involved in the second binding site are indicated by blue, magenta, and green triangles. m, *Mus musculus*; h, *Homo sapiens*; r, *Rattus norvegicus*; x, *Xenopus laevis*; z, *Danio rerio*.

The Primary Shank PDZ-Binding Target in Synapse Should be SAPAP. The high-affinity interaction between Shank N-PDZ and SAPAP E-PBM described above provides a biochemical basis for the specific Shank/SAPAP complex formation in synapses instead of many other reported Shank PDZ domain-mediated interactions. To further substantiate this conclusion, we measured the binding affinities of Shank PDZ with several of its reported synaptic target proteins, including neuroligin 1, neuroligin 3, and β-PIX. To ensure the coverage of possible extended sequences in both Shank PDZ and these targets, we used Shank3 SH3-PDZ and the entire C-terminal tails of neuroligin 1 (residues 720–843) and neuroligin 3 (residues 708–825), along with the coiled-coil PBM of β-PIX (residues 494–646), for quantitative ITC-based binding assays. All three reported Shank PDZ targets were found to bind to Shank SH3-PDZ with modest K_d values of several micromoles

(Fig. 1*D*), roughly 100-fold weaker than the Shank/SAPAP binding. Therefore, even under comparable concentrations, SAPAP would have a much higher priority for forming a complex with Shank than other coexisting proteins, such as neuroligins and β-PIX in synapses, not to mention that SAPAPs are among the most abundant proteins in PSD (8).

Structural Basis Governing the Specific Shank3 N-PDZ/SAPAP3 E-PBM Interaction.

Overall structure. To elucidate the molecular mechanism underlying the specific Shank/SAPAP interaction, we solved the crystal structure of the Shank3 N-PDZ/SAPAP3 E-PBM peptide complex at 2.5-Å resolution (Table S1). Other than the very N-terminal nine residues of Shank3 N-PDZ (residues 533–541), the residues from both N-PDZ and E-PBM can be clearly assigned

in the crystal electrodensity map. The complex in the crystal appears as a domain-swapped dimer with a twofold symmetry axis (Fig. 2A). The N-terminal extension (N-extension) of each PDZ domain forms a β-hairpin structure (βN1 and βN2) that interacts with the extension sequence of SAPAP3 E-PBM in the neighboring complex via antiparallel β-sheet augmentation on its one edge and with the elongated βB/βC loop (referred to as the BC loop hereinafter) of the PDZ domain on its other edge (Fig. 2A). The C-terminal PBM (i.e., the QTRL motif) binds to the canonical PDZ-binding pocket of Shank3 PDZ.

The Shank PDZ domain and its N-terminal β-hairpin extension are connected by a six-residue linker ([559]TSHSDY[564]), which is structured but does not participate in the SAPAP3 E-PBM binding (Fig. 2A). Detailed structural analysis also indicated no

intermonomer interaction, as well as very little energetic difference, for the Shank3 N-PDZ/SAPAP3 E-PBM complex to form either as a simple monomeric complex or as a domain-swapped dimer observed in the crystal (Fig. S1 A–C). Our static light-scattering analysis showed that Shank3 N-PDZ adopts a stable monomer in solution both before and after binding to SAPAP3 E-PBM (Fig. S1D); therefore, we did not differentiate the dimer or the monomer of the complex in our analysis, and considered the Shank3 N-PDZ/SAPAP3 E-PBM only as a monomeric complex.

Detailed interactions. The most unique feature of the Shank3 N-PDZ/SAPAP3 E-PBM complex structure is that the N-terminal extension and the elongated BC loop of N-PDZ directly interact with the N-terminal extension of SAPAP3 E-PBM, forming another hydrophobic core in addition to the canonical PDZ core

Fig. 2. Structural characterization of the specific interaction between Shank3 N-PDZ and SAPAP3 E-PBM. (A) Ribbon diagram representation of the Shank3 N-PDZ/SAPAP3 E-PBM complex crystal structure. Two Shank3 N-PDZs in the domain-swapped structure are colored in green and magenta; two SAPAP3 peptides are in cyan and yellow. (B) Surface map of Shank3 N-PDZ in the Shank3 N-PDZ/SAPAP3 E-PBM complex, showing two prominent hydrophobic pockets: the canonical PDZ binding pocket and the second binding pocket formed by the BC loop and N-extension of Shank3 PDZ for binding to the SAPAP3 upstream extension sequence. In the surface map, hydrophobic residues are in yellow, positive charged residues are in blue, and negative charged residues are in red. (C) Stereoview showing the detailed interactions between residues from the N-extension (magenta) and BC loop (green) of Shank3 and the SAPAP3 PBM extension (cyan). (D) Surface map representation showing that the Shank3 PDZ BC loop forms a prominent hydrophobic pocket for the interaction of several hydrophobic residues from the N-extension of PDZ (magenta) and the SAPAP3 peptide (cyan). (E) A 2Fo-Fc map of the BC loop of Shank3 N-PDZ in the N-PDZ/E-PBM complex structure showing that the electron densities of all residues can be clearly assigned. The map is calculated from the final PDB file and contoured at 1.0 σ. (F) Overlay of the Shank1 PDZ/SAPAP PBM complex (PDB ID code 1Q3P) with the Shank3 N-PDZ/SAPAP3 E-PBM complex. The dashed line represents several residues in the BC loop that were not defined in the Shank1 PDZ/SAPAP PBM complex structure. (G) Cartoon summarizing the binding mode between Shank3 N-PDZ and the SAPAP3 E-PBM peptide.

(Fig. 2 *B–D*). Specifically, the well-defined hydrophobic surface formed by the long BC loop (the longest BC loop among all PDZ domains; Fig. 2*E*) provides a docking site for the PDZ N-extension as well as the SAPAP3 PBM extension (Fig. 2 *C* and *D*). The SAPAP3 PBM extension [A(-14)~I(-7)] forms a β-strand anti-parallel to βN1 in the PDZ N-extension (Fig. S2). Analysis of the surface structure reveals that Shank3 N-PDZ contains two distinct hydrophobic pockets. One of these pockets is in the canonical PDZ domain accommodating the terminal hydrophobic Leu(0) of PBM, and the other, formed by N-terminal extension and the BC loop of N-PDZ, is responsible for specifically binding to Ile(-7) and Ile(-9) of SAPAP3 E-PBM (Fig. 2*B*, and summarized as a schematic diagram in Fig. 2*G*).

An overlay analysis of our Shank3 N-PDZ/SAPAP3 E-PBM complex structure with the structure of Shank1 PDZ in complex with a hexapeptide (EAQTRL) (61) revealed that the canonical PDZ/PBM interactions in the two structures are essentially identical (an rmsd value of 0.53Å in the PDZ region excluding the BC loop) (Fig. 2*F* and Fig. S3). The major differences between our structure and several previously determined canonical Shank PDZ structures are in their BC loops, which are partially flexible in all previously reported structures (Fig. S4). This structural analysis is fully consistent with our biochemistry data, showing that Shank3 N-PDZ contains an additional binding site outside the canonical PDZ domain. This newly identified binding site functions to recognize the extension sequences upstream the SAPAP3 PBM. Our structural data also provide a mechanistic explanation for the highly specific binding of Shank to SAPAP instead of to other reported Shank PDZ targets.

Validation of the Shank3 N-PDZ/SAPAP3 E-PBM Interaction. We next investigated the roles of three structural components, namely the BC loop and N-terminal β-hairpin extension of Shank3 PDZ and the SAPAP3 PBM extension, in the Shank3/SAPAP3 complex formation. To probe the role of the elongated BC loop of Shank3 PDZ, we deleted the majority of its BC loop (E591-L606) and left four residues (GAKA) of sufficient length to form a loop connecting βB and βC of the PDZ domain. We made this deletion using Shank3 SH3-PDZ for our quantitative binding assay (referred to as SH3-PDZ dBC). Deletion of the BC loop essentially eliminated all of the binding enhancement between Shank3 SH3-PDZ and SAPAP3 E-PBM afforded by the second binding site outside the canonical PDZ domain (K_d values of ~4.88 μM for the mutant vs. ~0.022 μM for the WT SH3-PDZ and 5.8 μM for the canonical PDZ domain) (Figs. 1*B* and 3*A*, A1 and A2). We then deleted the N-terminal β-hairpin extension of Shank3 PDZ (T543-Y564, denoted SH3-PDZ dEXT), and found that this deletion also decreased Shank3 SH3-PDZ binding to SAPAP3 E-PBM,
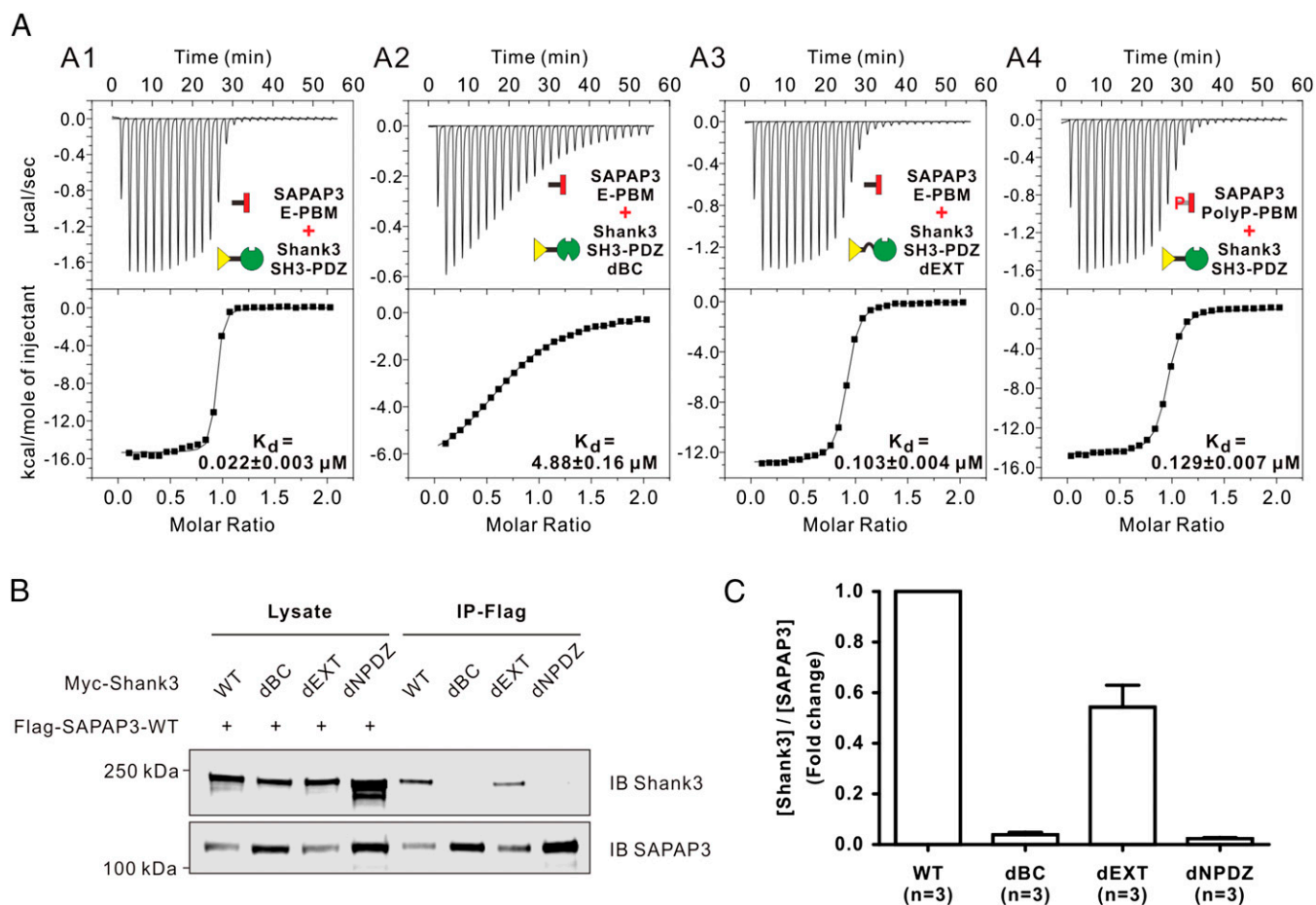

Fig. 3. Validation of the N-PDZ/E-PBM–mediated specific interaction between Shank3 and SAPAP3. (*A*) ITC-based measurements comparing the binding affinities between SAPAP3 E-PBM (WT or mutant) to Shank3 SH3-PDZ and its mutants. (*B* and *C*) Co-IP assay showing the importance of the specificity site on the full-length Shank3/SAPAP3 interaction. In *B*, cell lysates from HEK293T cells cotransfected with the full-length Flag-SAPAP3 and the full-length Myc-Shank3 WT (or its mutants) were immunoprecipitated by anti-Flag beads, and the resulting immunoprecipitates were immunoblotted for Shank3 and SAPAP3 as indicated. *C* shows quantification of co-IP results from three independent experiments. The intensity ratio of [Shank3]/[SAPAP3] in each co-IP lane (lanes 5–8) was calculated to indicate the interaction affinity, and compared with the signal ratio of the WT Shank3. Data are expressed as mean ± SEM.

albeit by a modest scale of approximately fivefold (Fig. 3*A*, A3). Finally, we replaced the extension sequence proceeding the PBM of SAPAP3 E-PBM (I966–I970) with five proline residues (referred to as PolyP-PBM), which were designed to disrupt the β-sheet formation of this segment with the β-hairpin extension of Shank3 N-PDZ (Fig. 2*A* and Fig. S2). Similar to the deletion of the β-hairpin extension from Shank3 N-PDZ, the SAPAP3 PolyP-PBM also exhibited approximately fivefold weaker binding to Shank3 SH3-PDZ (Fig. 3*A*, A4).

We then tested the role of the extension sequences in the second binding site observed in the N-PDZ/E-PBM complex to the binding between the full-length Shank3 and SAPAP3 expressed in heterologous cells. In this assay, we used N-terminal Flag-tagged SAPAP3 (Flag-SAPAP3; residues 1–977) to coimmunoprecipitate N-terminal Myc-tagged WT Shank3 (residues 1–1,730) or its mutants. As expected, the WT Shank3 showed a robust interaction with WT SAPAP3. Deletion of the BC loop from Shank3 reduced its binding to SAPAP3 to the background level, and deletion of the β-hairpin extension of Shank3 PDZ reduced its binding to SAPAP3 by ∼40%. As a control, deletion of the entire N-PDZ (residues 543–665) from Shank3 eliminated its binding to SAPAP3 (Fig. 3 *B* and *C*). We also used SAPAP3 WT or its E-PBM mutants to coimmunoprecipitate WT Shank3. Replacement of the PBM extension sequence with five proline residues (PolyP) weakened the binding of SAPAP3 to Shank3. Deleting the canonical PBM (the QTRL motif on SAPAP3, labeled "Δ4") eliminated the binding (Fig. S5*A*). A pull-down assay using purified GST-fused Shank3 SH3-PDZ to pull down the full-length SAPAP3 WT or its E-PBM mutants further supported the foregoing results (Fig. S5*B*). Taken together, our biochemical analyses indicate that all three components in the second binding site contribute to the strong and specific interaction between Shank3 and SAPAP3.

The Specific Shank3/SAPAP3 Interaction Is Critical for Shank3 Synaptic Targeting and Shank3-Mediated Synaptogenesis.

The interaction between Shank and SAPAP is known to be critical for Shank synaptic localization in cultured hippocampal neurons (7, 62). We used this assay to assess the role of the second binding site in the N-PDZ/E-PBM complex in Shank3 synaptic targeting. For convenience of imaging analysis, we used N-terminal GFP-tagged Shank3 WT and its mutants (WT, dBC, dEXT, and dNPDZ) in our assay. We first verified that all of these Shank3 constructs are expressed at comparable levels in heterologous cells, and that the impact of the mutations on SAPAP3 binding (Fig. S5*C*) are essentially the same as those seen when using the Myc-tagged Shank3 shown in Fig. 3. We then assessed the spine localizations of the four Shank3 constructs by transfecting Shank3 into cultured hippocampal neurons at day in vitro 14 (DIV14) and imaging the GFP signal of fixed neurons at DIV18. mCherry was cotransfected with GFP-Shank3 to fill the transfected neurons (Fig. 4*A*). The percentages of Shank3-enriched spines were calculated to evaluate the synaptic targeting of each Shank3 construct. For each group, a total of 17–21 neurons from three independent batches of cultures were quantified. Typically, three to five branches were chosen for each neuron, with each branch covering the length of an ∼60-μm segment. All imaging, as well as the subsequent electrophysiology experiments, were performed in a double-blinded fashion.

Consistent with previously reported findings (7, 62), WT GFP-Shank3 can efficiently target to dendritic spines. However, the three GFP-Shank3 mutants exhibited defects in synaptic localization, often with more puncta accumulating in the shaft region and much lower efficiency in localizing to dendritic spines (Fig. 4*A*). Quantification results showed 92.1 ± 1.7% (mean ± SEM, hereinafter) dendritic spines with GFP signal enrichment relative to the shaft region in WT GFP-Shank3 neurons. In contrast, only 57.9 ± 4.2% of the dendritic spines in dBC-Shank3 neurons and
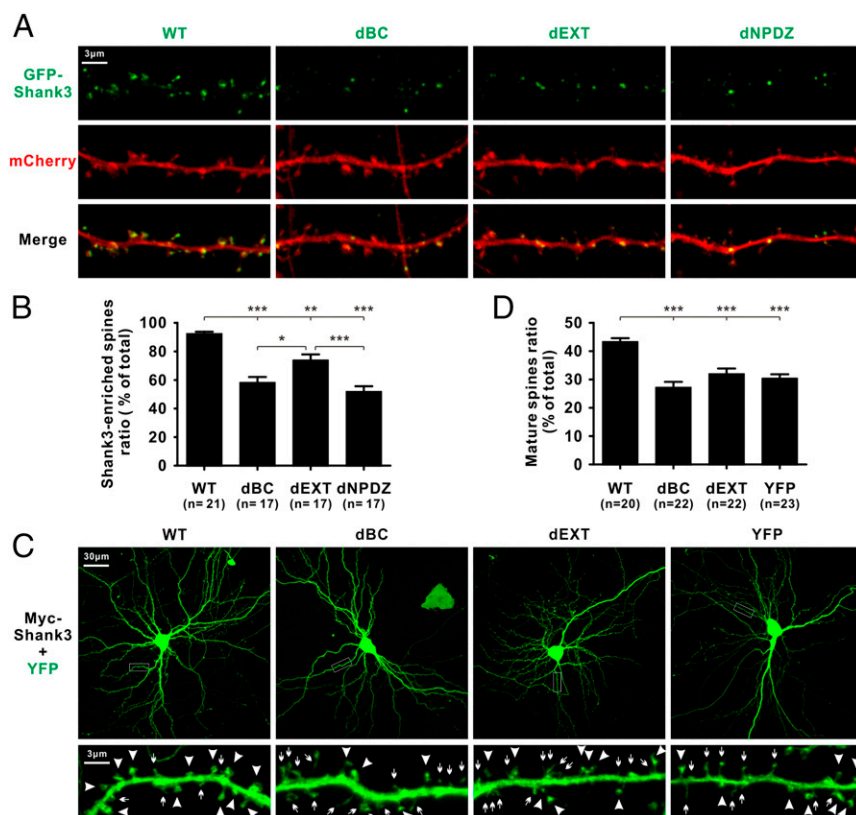

Fig. 4. The specific Shank3-SAPAP3 interaction is crucial for Shank3 synaptic localization and spine maturation in cultured hippocampal neurons. (*A* and *B*) Cultured hippocampal neurons were cotransfected with the full-length GFP-Shank3 WT or its mutants together with mCherry at DIV14, and imaged at DIV18. (*A*) Representative images. Spines with a stronger GFP-Shank3 signal than in the corresponding dendritic shaft region are referred to as Shank3-enriched spines. The percentage of Shank3-enriched spines over total spines was calculated to indicate Shank3 synaptic localization. (*B*) Quantification of the imaging data derived from 17–21 neurons from three independent batches of neuron cultures. Data are expressed as mean ± SEM. *$P < 0.05$; **$P < 0.01$; ***$P < 0.001$, one-way ANOVA with Tukey's multiple comparison test. (*C* and *D*) Cultured hippocampal neurons were cotransfected with the full-length Myc-Shank3 WT or its mutants together with YFP or YFP alone at DIV14, and imaged at DIV18. (*C*) Representative images. Spines with mushroom heads were counted as mature spines and indicated by a large arrowhead. Immature spines, including stubby, filopodia, branchy, and thin mushroom spines, are indicated by small arrows. (*D*) Quantification of the imaging data derived from 20–23 neurons from six independent batches of cultures. Data are expressed as mean ± SEM. ***$P < 0.001$, one-way ANOVA with Tukey's multiple comparison test.

73.6 ± 4.3% of those in dEXT-Shank3 neurons showed an enriched GFP signal. Complete disruption of the Shank3/SAPAP3 interaction by deletion of the entire N-PDZ (dNPDZ-Shank3) led to only 51.6 ± 4.1% dendritic spines with GFP signal enrichment (Fig. 4B) (*P < 0.05, **P < 0.01, and ***P < 0.001, one-way ANOVA with Tukey's multiple comparison test). This result indicates that the high affinity and specific complex formation between Shank3 and SAPAP3 mediated by the N-PDZ/ E-PBM interaction is required for Shank3 synaptic localization in cultured hippocampal neurons.

We next evaluated the roles of the specific Shank3/SAPAP3 interaction on Shank3-induced synaptogenesis. In this assay, we used Myc-tagged Shank3 as shown in Fig. 3B, and used YFP as the cell fill and the background transfection control. E16.5 mice primary hippocampal neurons were cultured, transfected at DIV14, and fixed at DIV18 for imaging YFP signals (Fig. 4C). A total of ~20 neurons for each group were analyzed from six independent batches of neuron cultures (Fig. 4D) using the same branch selection criteria as in Fig. 4A. The spine morphology analysis was performed in a blinded manner by two individuals using different strategies. The first approach uses visual inspection to classify spines with a mushroom-like head as mature spines (indicated by the large arrowheads in Fig. 4C) and spines with other morphologies, such as filopodia-like, stubby, branchy, and thin mushroom (i.e., long neck and small head) as immature spines (indicated by the small arrows in Fig. 4C). In the second strategy, the head width, neck width, and spine length of each spine were measured using ImageJ. A spine with a head width 2.5 times larger than the neck width and a spine length smaller than 3.0 times the head width is classified as a mature spine. These criteria were chosen to ensure a mushroom-like head and to exclude spines with a thin mushroom shape and a long neck from being classified as mature spines.

These two methods generated essentially same results within statistical error. Here we present only the results generated by the second strategy for comparison and analysis. At DIV18, the control neurons (the YFP alone group) had 30.3 ± 1.6% of the dendritic spines classified as mature spines. Overexpression of Shank3 WT promotes dendritic spine maturation by significantly increasing the percentage of mature spines to 43.2 ± 1.4%, a finding consistent with previous studies (62, 63). In contrast, overexpression of Shank3 mutants failed to promote dendritic spine maturation compared with the WT Shank3. The dBC-Shank3–expressing neurons and the dEXT-Shank3–expressing neurons contained 27.1 ± 2.1% and 31.9 ± 2.1% mature spines, respectively (Fig. 4D) (***P < 0.001, one-way ANOVA with Tukey's multiple comparison test).

The foregoing results indicate that the N-PDZ/E-PBM–mediated specific Shank3/SAPAP3 interaction, most likely via efficient targeting of Shank3 to dendritic spines, is important for the role of Shank3 in promoting synaptogenesis. It is formally possible that the observed synaptic targeting defects of Shank constructs bearing N-PDZ mutations might have resulted from unexpected dominant negative interactions of the mutant PDZ domains with certain unknown proteins.

Disruption of the Shank3/SAPAP3 Interaction by Specific Inhibitory Peptide Weakens Synaptic Activity. We next wished to directly test the possible impact of a disrupted Shank/SAPAP interaction on the synaptic activity in cultured neurons. The discovery of the potent and specific binding of the last 15 residues of SAPAP3 (referred to as 15AA hereinafter) to Shank N-PDZ offers a unique opportunity to use this short peptide as a specific inhibitor blocking the Shank3/SAPAP3 complex formation in neurons. In addition, because all family members of Shank and SAPAP contain essentially the same N-PDZ and E-PBM, respectively (Fig. 1 E and F), the 15AA SAPAP3-CT peptide

should be able to disrupt all Shank/SAPAP interactions when delivered to synapses.

We first tested whether this 15AA peptide can block the Shank/ SAPAP interaction when expressed in heterologous cells. An expression construct fusing 15AA to the C terminus of YFP driven by the CMV promoter was used to express YFP-15AA in HEK293T cells. When mixed individually, GST-fused Shank3 SH3-PDZ can robustly pull down either YFP-15AA or Flag-SAPAP3 from the cell lysates expressing each protein with comparable binding affinities (Fig. 5A, lanes 3 and 4). We next tested whether YFP-15AA can compete with the full-length SAPAP3 for binding to Shank3. For such competition assay, we kept Flag-SAPAP3 cell lysates at a fixed amount in the reaction mixture and gradually increased the YFP-15AA dosage as indicated. The results show that an increasing amount of YFP-15AA was pulled down by GST-Shank3. Correspondingly, the amount of Flag-SAPAP3 bound to Shank3 continued to decrease to near disappearance (Fig. 5A, lanes 4–8).

To ensure the specificity of the competition, we repeated the same experiments using YFP-15AA lacking the last four residues corresponding to the PBM motif (referred to as YFP-15d4), because this peptide essentially has no binding to Shank3 (Fig. 1C). As expected, GST-Shank3-SH3-PDZ failed to pull down YFP-15d4 at all dosages tested (Fig. 5B, lane 3). Therefore, even at the highest dosage used, YFP-15d4 had no detectable impact on the interaction between Shank3-SH3-PDZ and SAPAP3 (Fig. 5B), further confirming the specificity of YFP-15AA in blocking the Shank/SAPAP interaction.

Given that the 15AA blocking peptide can effectively disrupt the Shank3/SAPAP3 interaction in heterologous cells, we next investigated whether 15AA can effectively modulate synaptic activity when expressed in synapses. To test this, the blocking peptide (YFP-15AA), control peptide (YFP-15d4) and YFP alone expression vectors were packaged in recombinant adeno-associated virus (AAV). The expression of these peptides was driven by the human synapsin promoter for their specific neuronal expression. Postnatal day 0 (P0) mice primary hippocampal neurons were cultured and infected with AAV at DIV07. At DIV18–20, miniature excitatory synaptic currents (mEPSCs) of YFP-positive neurons were recorded. For each group, 11–17 neurons from five separate batches were recorded and analyzed. The amplitudes of mEPSCs in neurons expressing YFP-15AA were significantly reduced compared with those expressing either YFP or YFP-15d4 (Fig. 5 D and F). The mEPSC frequencies showed no significant differences in the three groups of neurons (Fig. 5 E and G). The electrophysiological data indicate that the delivery of the 15AA peptide into neurons, most likely through disrupting the synaptic Shank/SAPAP interaction, can weaken the excitatory synaptic strength, presumably by reducing the number of functional AMPA receptors in each spine (Fig. 5H). Of course, we cannot rule out the possibility that the 15AA peptide may also target as-yet unknown PDZ domains proteins in neurons.

Discussion

In this study, we have discovered a previously unrecognized mode of PDZ domain/target interaction that governs the highly specific interaction between Shank and SAPAP, two major scaffold proteins that are vital for both synapse development and synaptic activity regulations. Our quantitative binding affinity comparisons indicate that the binding of Shank PDZ to SAPAP is of several hundred-fold stronger than that of Shank PDZ to many other previously reported binding proteins. Our biochemical analysis predicts that essentially all Shank PDZ domains are occupied by SAPAP, and that very few other proteins can compete with SAPAP for forming complex with Shank. Our study also provides a mechanistic explanation for the overlapping disease phenotypes caused by mutations in *SAPAP* and *Shank* in humans.
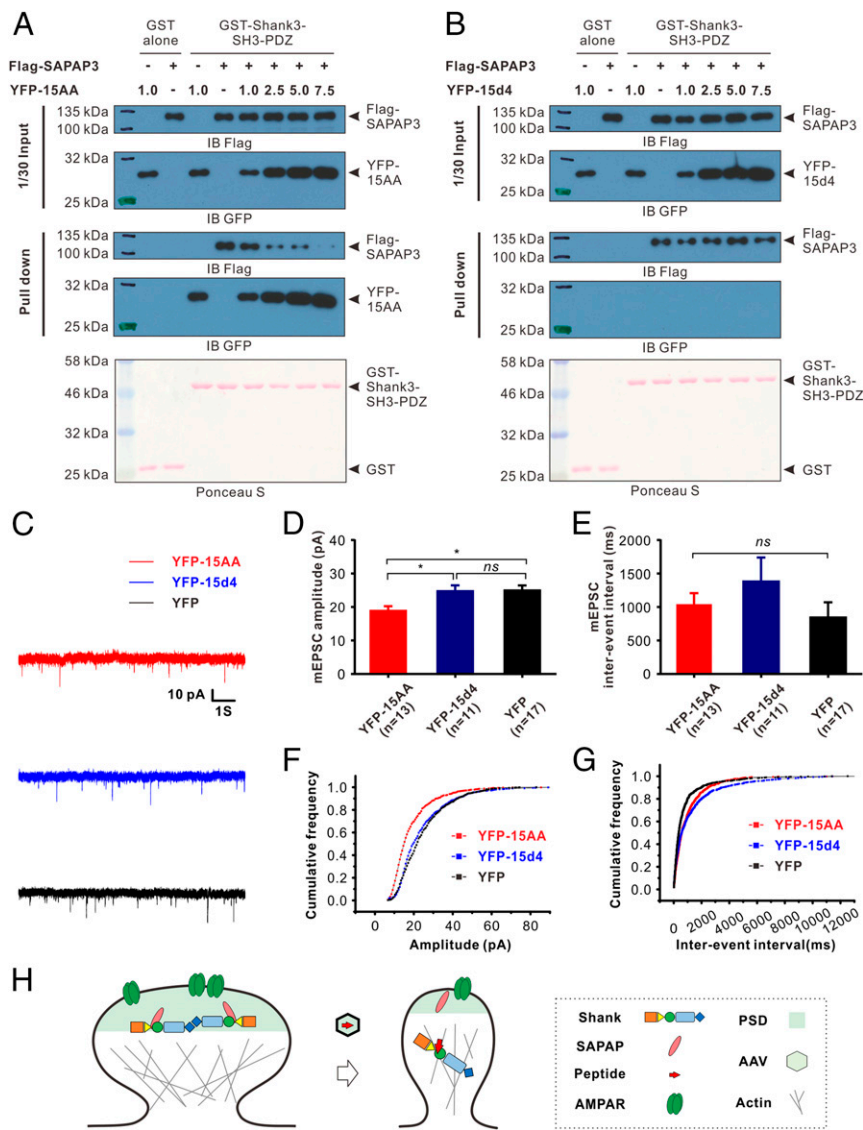
Fig. 5. SAPAP3-CT peptide is able to disrupt the Shank3-SAPAP3 interaction and weaken excitatory synaptic activity in cultured hippocampal neurons. (*A* and *B*) Pull-down–based competition experiment showing that the 15AA SAPAP3-CT peptide can effectively disrupt the Shank3-SAPAP3 interaction (*A*), whereas the control peptide lacking the last four-residue PBM cannot (*B*). (*C*–*E*) Cultured hippocampal neurons were infected with AAVs expressing YFP-15AA, YFP-15d4, or YFP alone at DIV07, and mEPSCs were recorded at DIV18–20. The blocking peptide significantly reduced neurotransmission, whereas the control peptide failed to do so. Data shown are representative of five independent batches. (*C*) Representative mEPSC traces. (*D* and *E*) Quantification of mEPSC amplitude (*D*) and interevent interval (*E*), which is inversely proportional to frequency. Data are expressed as mean ± SEM. *$P < 0.05$; ns, not significantly different, one-way ANOVA with Tukey's multiple comparison test. (*F* and *G*) Cumulative distribution of mEPSC amplitude (*F*) and interevent interval (*G*). (*H*) Cartoon illustrating a proposed working model of the Shank/SAPAP interaction blocking peptide in regulating synapse formation and synaptic activity.

The structures of the Shank3 N-PDZ and SAPAP3 E-PBM complexes determined in this study reveal that both the specificity and enhanced binding affinity between Shank and SAPAP originate from a unique binding site outside the canonical Shank PDZ and the canonical SAPAP PBM. A highly conserved N-terminal extension sequence of Shank PDZ forms a β-hairpin structure and specifically interacts with a conserved, SAPAP-specific sequence upstream of its PBM to form the second binding site. Given that other reported Shank-binding proteins, such as neuroligins and β-PIX contain only canonical PBMs but not residues that can bind to the second specificity site in Shank N-PDZ, these proteins bind to Shank with much lower affinities compared with SAPAP. Our structural analysis not only provides a mechanistic explanation to the highly specific interaction between Shank PDZ and its functional target SAPAP, but also may identify a more general mechanism governing many other PDZ domain/target interactions. Emerging evidence suggests that many PDZ domains contain extension sequences at their two termini that are highly conserved and predicted to form secondary structures (60, 64). These extension sequences often can function together with the canonical PDZ domain to form another target binding site in addition to the common αB/βB groove in all PDZ domains (65, 66). Be-

cause such extension sequences are highly specific to each individual PDZ domain, the corresponding target binding sites formed by the extension sequences are also likely to be distinct for each PDZ domain. Therefore, such additional target binding site formed by the extension sequence can be regarded as the specificity site of a PDZ domain, which provides a mechanistic basis for a given PDZ domain to bind to its cognate targets with high specificity. We believe that many PDZ/target interactions occurring in living cells should be specific and with high affinity instead of promiscuous and with modest affinity as is generally perceived.

PDZ domain proteins are particularly abundant in synapses, and even larger numbers of PDZ domain binding targets are known to coexist in the small spaces of dendritic spines in synapses (6, 67, 68). Quite often, each PDZ domain from various synaptic scaffold proteins (e.g., any PDZ domain from the DLG family MAGUKs or the Shank PDZ described here in detail) has been reported to bind to many (up to several dozen) different target proteins. Such promiscuous PDZ/target interactions are conceptually not compatible with specific cellular functions of either PDZ domain proteins or their reported binding targets in living animals; therefore, careful biochemical and structural studies of PDZ and target interactions as described here will have

an important role in the future. In addition, our study also suggests the possibility that similar extension sequence-mediated affinity enhancements may exist in other reported protein module/target interactions reported in the literature.

The discovery that a 15-residue peptide derived from SAPAP3 C-terminal tail can specifically block the Shank/SAPAP complex formation and modulate synaptic activity provides a proof of concept for manipulating the Shank/SAPAP interaction in living organisms. Such an inhibitory peptide should be able to down-tune the excitatory synaptic activity by selectively inhibiting SAPAP/Shank complex formation. In principle, this inhibitory peptide may be useful for modulating synaptic activities in patients with an undesired level of excitatory circuit activation, such as caused by *Shank* gene duplication (47).

Materials and Methods

Constructs and Protein Expression. Various coding sequences of *Shank3* and *SAPAP3* were PCR-amplified from the mouse full-length genes *Shank3* and *SAPAP3*, kindly provided by Guoping Feng, Massachusetts Institute of Technology, Cambridge, MA. Residue numbers indicated in the study refer to the full-length Shank3 (BAE16756; 1,730 residues) and SAPAP3 (NP_941020; 977 residues). Genes encoding β-PIX coiled-coil PBM (residues 494–646; NP_059098.2), neuroligin 1 tail (residues 720–843, NP_619607.2) and neuronligin 3 tail (residues 708–825; NP_766520.2) were individually amplified by PCR from a mouse cDNA library. PCR products were cloned into in-house modified pET32a vectors or pGEX-4T-1 vector for protein expression. Recombinant proteins were expressed in *Escherichia coli* BL21 (DE3) cells in LB medium at 16 °C. N-terminal thioredoxin (TRX)-His$_6$–tagged or His$_6$-tagged recombinant proteins were purified using a nickel-NTA affinity column, followed by size-exclusion chromatography. When needed, TRX-His$_6$-tag and His$_6$-tag were cleaved by HRV 3C protease and separated by size-exclusion chromatography. N-terminal GST-tagged recombinant proteins were purified by a glutathione Sepharose affinity column, followed by size-exclusion chromatography. Peptides containing SAPAP3 PBM (last six residues) for ITC analysis or E-PBM (last 15 residues) for crystal screening were commercially synthesized. For heterologous cell or neuronal expression, the full-length *Shank3* and *SAPAP3* genes, either WT or mutants, were cloned into pCMV-Myc, pcDNA3.1-Flag, or pEGFP-C3 vectors.

ITC Assays. ITC measurements were carried out on a MicroCal VP-ITC calorimeter at 25 °C in buffer containing 50 mM Tris pH 8.0, 100 mM NaCl, 1 mM EDTA, and 1 mM DTT. High-concentration proteins or peptides (concentration of 300 μM) were loaded into the syringe and titrated into the cell containing low-concentration (30 μM) proteins. Titration data were analyzed using Origin 7.0 and fitted by a one-site binding model.

Crystallization and Data Collection and Processing. Crystals of Shank3 N-PDZ in complex with the SAPAP3 E-PBM peptide were obtained by the hanging-drop vapor diffusion method at 16 °C. The Shank3 N-PDZ/SAPAP3 E-PBM complex crystal was grown in solution containing 0.1 M Bis-Tris pH 5.5 and 3.0 M NaCl. Glycerol [25% (vol/vol)] was added as an cryoprotectant. X-ray data were collected at beamline BL17U1 of the Shanghai Synchrotron Radiation Facility. The diffraction data were processed and scaled by HKL2000 (69).

Using the structure of the Shank1 PDZ domain (PDB ID code 1Q3O) as the search model, the initial structural model was solved using the molecular replacement method in PHASER (70). The model was then refined by the phenix.refinement (71). Coot (72) was used for peptide modeling and model adjustments. TLS refinement was applied at the final refinement stage. The final structure was validated by phenix.model_vs_data (71) validation tools. The structure figures were prepared using PyMOL (pymol.sourceforge.net/).

Analytical Gel Filtration Chromatography Coupled with Static Light Scattering. This analysis was performed on a fast protein liquid chromatography (FPLC) system coupled with a static light-scattering detector (miniDAWN; Wyatt) and a differential refractive index detector (Optilab; Wyatt). Protein samples (100 μL, concentration of 100 μM) were loaded into a Superose 12 10/300 GL column preequilibrated with assay buffer containing 50 mM Tris pH 8.0, 100 mM NaCl, 1 mM EDTA, and 1 mM DTT on an AKTA FPLC system (GE Healthcare). Data were analyzed with Astra 6 (Wyatt).

Coimmunoprecipitation and GST Pulldown Assays. For the coimmunoprecipitation (co-IP) assays, in each reaction, 20 μL of anti-Flag M2 magnetic beads

(Sigma-Aldrich) were incubated with cell lysates for 2 h at room temperature to immunoprecipitate overexpressed Flag-tagged proteins. For the GST pull-down assay, 25 μL of glutathione Sepharose beads charged with 0.05–0.2 nmol purified GST-tagged proteins or GST alone was used to pull down the intended proteins for each reaction. After extensive washing, captured proteins were eluted by SDS/PAGE sample buffer by boiling, resolved by 4–15% (wt/vol) gradient Mini-PROTEAN TGX gels (Bio-Rad), and immunoblotted with specific antibodies. In the co-IP assays, the membranes were scanned and signal intensities were analyzed using an Odyssey CLx infrared imaging system (LI-COR Biosciences). In the pull-down assays, protein signals were visualized by an HRP-conjugated secondary antibody (Pierce) and SuperSignal (Pierce).

Primary Hippocampal Neuron Culture. Primary hippocampal neuron cultures were prepared from E16.5 C57BL/6 WT mice hippocampi (for transfection/imaging) or P0 C57BL/6 WT mice hippocampi (for AAV-infection/electrophysiology). Cells were seeded on coverslips successively coated by poly-D-lysine (Sigma-Aldrich) and laminin (Sigma-Aldrich) in 12-well plates. Cultures were maintained for 18–20 d in vitro in Neurobasal medium (for E16.5 neurons) or Neurobasal A medium (for P0 neurons) (Gibco) supported by 1× GlutaMax and 2% (wt/vol) B27 supplement (Gibco). For E16.5 neuron culture, cells were transfected or cotransfected at DIV14 with 2 μg plasmids per well using Lipofectamine 2000 reagent (Invitrogen). Cells were fixed at DIV18 with 4% (vol/vol) paraformaldehyde (PFA) together with 4% (wt/vol) sucrose in 1× PBS (pH 7.5) and then mounted on slides for imaging. For P0 neuron culture, AAV was treated at DIV07 to ensure that >20% neurons in each well were infected.

Microscopy. Neuronal images were acquired on a Leica SP8 confocal microscope with a 40× oil-immersion lens. For detailed dendritic branch and spine imaging, an additional 5× zoom factor was applied. Secondary and tertiary dendritic branches with appropriate shaft width were selected for analysis. On average, between three and five branches were selected at random to represent each neuron. For each branch, a length of ∼60 μm was imaged, and all spines within this section were analyzed. Multiple optical sections in the z-dimension (neuron, 20–40 sections; branch, 10–20 sections) at 0.35-μm z-intervals were collected and projected to a 2D image using a maximum intensity operation. Synaptic localization was analyzed according to the 2D projection images. Spine morphology was analyzed according to the 2D projection images together with Z-section checking.

Whole-Cell Recordings and mEPSC Analysis. Patch-clamp experiments were performed on cultured hippocampal neurons at DIV18–20. The culture medium was exchanged with an extracellular solution containing 124 mM NaCl, 26 mM NaHCO$_3$, 10 mM glucose, 2.5 mM KCl, 1.25 mM NaH$_2$PO$_4$, 2 mM CaCl$_2$, and 2 mM MgSO$_4$, saturated with 95% O$_2$–5% CO$_2$ (pH 7.4, 295–305 mOsm). Recording pipettes were pulled (P-97 micropipette puller; Sutter Instrument) from standard-wall borosilicate glass without filament (o.d. 1.5 mm; Sutter Instrument). The pipette-to-bath DC resistance of patch electrodes ranged from 3.0 to 5 MΩ with a pipette solution containing 130 mM CH$_3$O$_3$SCs, 10 mM Hepes, 5 mM NaCl, 1 mM MgCl$_2$, 0.2 mM EGTA, 5 mM QX-314, 2 mM MgATP, and 0.1 mM Na-GTP, with pH adjusted to 7.2 with CsOH and osmolality adjusted to ∼300 mOsm/L. mEPSCs were pharmacologically isolated by blocking the GABA receptor with picrotoxin (100 μM) and blocking the action potential generation with tetrodotoxin (1 μM). Recordings were obtained using a MultiClamp 700B amplifier (Molecular Devices). Analog signals were low-pass Bessel-filtered at 2 kHz and digitized at 10 kHz through a Digidata 1440A interface (Molecular Devices). The membrane potential was held at −70 mV at 25 °C for 0.5–1.5 h after the culture was removed from the incubator. Data analysis was performed with Clampfit 10.2 (Molecular Devices) and MiniAnalysis 6.0 (Synaptosoft). Approximately 5 min of recording time was used for the mEPSC analysis.

Statistics. Statistical analyses were performed using one-way ANOVA with Tukey's multiple comparison test using GraphPad Prism software.

1. Blomberg F, Cohen RS, Siekevitz P (1977) The structure of postsynaptic densities isolated from dog cerebral cortex, II: Characterization and arrangement of some of the major proteins within the structure. *J Cell Biol* 74(1):204–225.

2. Carlin RK, Grab DJ, Cohen RS, Siekevitz P (1980) Isolation and characterization of postsynaptic densities from various brain regions: Enrichment of different types of postsynaptic densities. *J Cell Biol* 86(3):831–845.

3. Cohen RS, Blomberg F, Berzins K, Siekevitz P (1977) The structure of postsynaptic densities isolated from dog cerebral cortex, I: Overall morphology and protein composition. *J Cell Biol* 74(1):181–203.

4. Harris KM, Weinberg RJ (2012) Ultrastructure of synapses in the mammalian brain. *Cold Spring Harb Perspect Biol* 4(5):a005587.

5. Chen X, et al. (2008) Organization of the core structure of the postsynaptic density. *Proc Natl Acad Sci USA* 105(11):4453–4458.

6. Kim E, Sheng M (2004) PDZ domain proteins of synapses. *Nat Rev Neurosci* 5(10):771–781.

7. Naisbitt S, et al. (1999) Shank, a novel family of postsynaptic density proteins that binds to the NMDA receptor/PSD-95/GKAP complex and cortactin. *Neuron* 23(3):569–582.

8. Sheng M, Hoogenraad CC (2007) The postsynaptic architecture of excitatory synapses: A more quantitative view. *Annu Rev Biochem* 76:823–847.

9. Garner CC, Nash J, Huganir RL (2000) PDZ domains in synapse assembly and signalling. *Trends Cell Biol* 10(7):274–280.

10. El-Husseini AE, Schnell E, Chetkovich DM, Nicoll RA, Bredt DS (2000) PSD-95 involvement in maturation of excitatory synapses. *Science* 290(5495):1364–1368.

11. Kim E, et al. (1997) GKAP, a novel synaptic protein that interacts with the guanylate kinase-like domain of the PSD-95/SAP90 family of channel clustering molecules. *J Cell Biol* 136(3):669–678.

12. Takeuchi M, et al. (1997) SAPAPs: A family of PSD-95/SAP90-associated proteins localized at postsynaptic density. *J Biol Chem* 272(18):11943–11951.

13. Satoh K, et al. (1997) DAP-1, a novel protein that interacts with the guanylate kinase-like domains of hDLG and PSD-95. *Genes Cells* 2(6):415–424.

14. Ting JT, Peça J, Feng G (2012) Functional consequences of mutations in postsynaptic scaffolding proteins and relevance to psychiatric disorders. *Annu Rev Neurosci* 35(1):49–71.

15. Tu JC, et al. (1999) Coupling of mGluR/Homer and PSD-95 complexes by the Shank family of postsynaptic density proteins. *Neuron* 23(3):583–592.

16. Levy JM, Chen X, Reese TS, Nicoll RA (2015) Synaptic consolidation normalizes AMPAR quantal size following MAGUK loss. *Neuron* 87(3):534–548.

17. Zhu J, Shang Y, Zhang M (2016) Mechanistic basis of MAGUK-organized complexes in synaptic development and signalling. *Nat Rev Neurosci* 17(4):209–223.

18. Nair D, et al. (2013) Super-resolution imaging reveals that AMPA receptors inside synapses are dynamically organized in nanodomains regulated by PSD95. *J Neurosci* 33(32):13204–13224.

19. Kim E, Cho KO, Rothschild A, Sheng M (1996) Heteromultimerization and NMDA receptor-clustering activity of Chapsyn-110, a member of the PSD-95 family of proteins. *Neuron* 17(1):103–113.

20. Pinto D, et al. (2010) Functional impact of global rare copy number variation in autism spectrum disorders. *Nature* 466(7304):368–372.

21. Sato D, et al. (2012) SHANK1 deletions in males with autism spectrum disorder. *Am J Hum Genet* 90(5):879–887.

22. Crane J, et al. (2011) Family-based genetic association study of DLGAP3 in Tourette Syndrome. *Am J Med Genet B* 156B(1):108–114.

23. Bienvenu OJ, et al. (2009) Sapap3 and pathological grooming in humans: Results from the OCD collaborative genetics study. *Am J Med Genet B* 150B(5):710–720.

24. Züchner S, et al. (2009) Multiple rare SAPAP3 missense variants in trichotillomania and OCD. *Mol Psychiatry* 14(1):6–9.

25. Stewart SE, et al.; North American Brain Expression Consortium; UK Brain Expression Database (2013) Genome-wide association study of obsessive-compulsive disorder. *Mol Psychiatry* 18(7):788–798.

26. Feyder M, et al. (2010) Association of mouse Dlg4 (PSD-95) gene deletion and human DLG4 gene variation with phenotypes relevant to autism spectrum disorders and Williams' syndrome. *Am J Psychiatry* 167(12):1508–1517.

27. Kirov G, et al. (2012) De novo CNV analysis implicates specific abnormalities of postsynaptic signalling complexes in the pathogenesis of schizophrenia. *Mol Psychiatry* 17(2):142–153.

28. Wilson HL, et al. (2003) Molecular characterisation of the 22q13 deletion syndrome supports the role of haploinsufficiency of SHANK3/PROSAP2 in the major neurological symptoms. *J Med Genet* 40(8):575–584.

29. Sheng M, Kim E (2011) The postsynaptic organization of synapses. *Cold Spring Harb Perspect Biol* 3(12):a005678.

30. MacGillavry HD, Song Y, Raghavachari S, Blanpied TA (2013) Nanoscale scaffolding domains within the postsynaptic density concentrate synaptic AMPA receptors. *Neuron* 78(4):615–622.

31. Dani A, Huang B, Bergan J, Dulac C, Zhuang X (2010) Superresolution imaging of chemical synapses in the brain. *Neuron* 68(5):843–856.

32. MacGillavry HD, Hoogenraad CC (2015) The internal architecture of dendritic spines revealed by super-resolution imaging: What did we learn so far? *Exp Cell Res* 335(2):180–186.

33. Zhu J, et al. (2011) Guanylate kinase domains of the MAGUK family scaffold proteins as specific phospho-protein-binding modules. *EMBO J* 30(24):4986–4997.

34. Peça J, et al. (2011) Shank3 mutant mice display autistic-like behaviours and striatal dysfunction. *Nature* 472(7344):437–442.

35. Bozdagi O, et al. (2010) Haploinsufficiency of the autism-associated Shank3 gene leads to deficits in synaptic function, social interaction, and social communication. *Mol Autism* 1(1):15.

36. Wang X, et al. (2011) Synaptic dysfunction and abnormal behaviors in mice lacking major isoforms of Shank3. *Hum Mol Genet* 20(15):3093–3108.

37. Welch JM, et al. (2007) Cortico-striatal synaptic defects and OCD-like behaviours in Sapap3-mutant mice. *Nature* 448(7156):894–900.

38. Jiang-Xie LF, et al. (2014) Autism-associated gene Dlgap2 mutant mice demonstrate exacerbated aggressive behaviors and orbitofrontal cortex deficits. *Mol Autism* 5:32.

39. Schmeisser MJ, et al. (2012) Autistic-like behaviours and hyperactivity in mice lacking ProSAP1/Shank2. *Nature* 486(7402):256–260.

40. Won H, et al. (2012) Autistic-like social behaviour in Shank2-mutant mice improved by restoring NMDA receptor function. *Nature* 486(7402):261–265.

41. Jiang YH, Ehlers MD (2013) Modeling autism by SHANK gene mutations in mice. *Neuron* 78(1):8–27.

42. Prasad C, et al. (2000) Genetic evaluation of pervasive developmental disorders: The terminal 22q13 deletion syndrome may represent a recognizable phenotype. *Clin Genet* 57(2):103–109.

43. Precht KS, et al. (1998) Two 22q telomere deletions serendipitously detected by FISH. *J Med Genet* 35(11):939–942.

44. Manning MA, et al. (2004) Terminal 22q deletion syndrome: A newly recognized cause of speech and language disability in the autism spectrum. *Pediatrics* 114(2):451–457.

45. Jeffries AR, et al. (2005) Molecular and phenotypic characterization of ring chromosome 22. *Am J Med Genet A* 137(2):139–147.

46. Cook EH, Jr, Scherer SW (2008) Copy-number variations associated with neuropsychiatric conditions. *Nature* 455(7215):919–923.

47. Han K, et al. (2013) SHANK3 overexpression causes manic-like behaviour with unique pharmacogenetic properties. *Nature* 503(7474):72–77.

48. Darnell JC, et al. (2011) FMRP stalls ribosomal translocation on mRNAs linked to synaptic function and autism. *Cell* 146(2):247–261.

49. Gingras AC, Raught B, Sonenberg N (2001) Regulation of translation initiation by FRAP/mTOR. *Genes Dev* 15(7):807–826.

50. Tavazoie SF, Alvarez VA, Ridenour DA, Kwiatkowski DJ, Sabatini BL (2005) Regulation of neuronal morphology and function by the tumor suppressors Tsc1 and Tsc2. *Nat Neurosci* 8(12):1727–1734.

51. Yi JJ, et al. (2015) An autism-linked mutation disables phosphorylation control of UBE3A. *Cell* 162(4):795–807.

52. Volk L, Chiu SL, Sharma K, Huganir RL (2015) Glutamate synapses in human cognitive disorders. *Annu Rev Neurosci* 38:127–149.

53. Zhou Y, et al. (2016) Mice with Shank3 mutations associated with ASD and schizophrenia display both shared and distinct defects. *Neuron* 89(1):147–162.

54. Meyer G, Varoqueaux F, Neeb A, Oschlies M, Brose N (2004) The complexity of PDZ domain-mediated interactions at glutamatergic synapses: A case study on neuroligin. *Neuropharmacology* 47(5):724–733.

55. Park E, et al. (2003) The Shank family of postsynaptic density proteins interacts with and promotes synaptic accumulation of the beta PIX guanine nucleotide exchange factor for Rac1 and Cdc42. *J Biol Chem* 278(21):19220–19229.

56. Olson PA, et al. (2005) G-protein-coupled receptor modulation of striatal CaV1.3 L-type Ca2+ channels is dependent on a Shank-binding domain. *J Neurosci* 25(5):1050–1062.

57. Zhang H, et al. (2005) Association of CaV1.3 L-type calcium channels with Shank. *J Neurosci* 25(5):1037–1049.

58. Kreienkamp HJ, Zitzer H, Gundelfinger ED, Richter D, Bockers TM (2000) The calcium-independent receptor for alpha-latrotoxin from human and rodent brains interacts with members of the ProSAP/SSTRIP/Shank family of multidomain proteins. *J Biol Chem* 275(42):32387–32390.

59. Im YJ, et al. (2010) Structural basis for asymmetric association of the betaPIX coiled coil and shank PDZ. *J Mol Biol* 397(2):457–466.

60. Ye F, Zhang M (2013) Structures and target recognition modes of PDZ domains: Recurring themes and emerging pictures. *Biochem J* 455(1):1–14.

61. Im YJ, et al. (2003) Crystal structure of the Shank PDZ-ligand complex reveals a class I PDZ interaction and a novel PDZ-PDZ dimerization. *J Biol Chem* 278(48):48099–48104.

62. Sala C, et al. (2001) Regulation of dendritic spine morphology and synaptic function by Shank and Homer. *Neuron* 31(1):115–130.

63. Roussignol G, et al. (2005) Shank expression is sufficient to induce functional dendritic spine synapses in aspiny neurons. *J Neurosci* 25(14):3560–3570.

64. Wang CK, Pan L, Chen J, Zhang M (2010) Extensions of PDZ domains as important structural and functional elements. *Protein Cell* 1(8):737–751.

65. Bhattacharya S, et al. (2010) A conformational switch in the scaffolding protein NHERF1 controls autoinhibition and complex formation. *J Biol Chem* 285(13):9981–9994.

66. Yan J, Pan L, Chen X, Wu L, Zhang M (2010) The structure of the harmonin/sans complex reveals an unexpected interaction mode of the two Usher syndrome proteins. *Proc Natl Acad Sci USA* 107(9):4040–4045.

67. Feng W, Zhang M (2009) Organization and dynamics of PDZ-domain-related supramodules in the postsynaptic density. *Nat Rev Neurosci* 10(2):87–99.

68. Bayés À, et al. (2014) Human post-mortem synapse proteome integrity screening for proteomic studies of postsynaptic complexes. *Mol Brain* 7(1):88.

69. Otwinowski Z, Minor W (1997) Processing of X-ray diffraction data collected in oscillation mode. *Methods Enzymol* 276:307–326.

70. McCoy AJ, et al. (2007) Phaser crystallographic software. *J Appl Cryst* 40(Pt 4):658–674.

71. Adams PD, et al. (2010) PHENIX: A comprehensive Python-based system for macromolecular structure solution. *Acta Crystallogr D Biol Crystallogr* 66(Pt 2):213–221.

72. Emsley P, Lohkamp B, Scott WG, Cowtan K (2010) Features and development of Coot. *Acta Crystallogr D Biol Crystallogr* 66(Pt 4):486–501.

Supporting Information

Zeng et al. 10.1073/pnas.1523265113
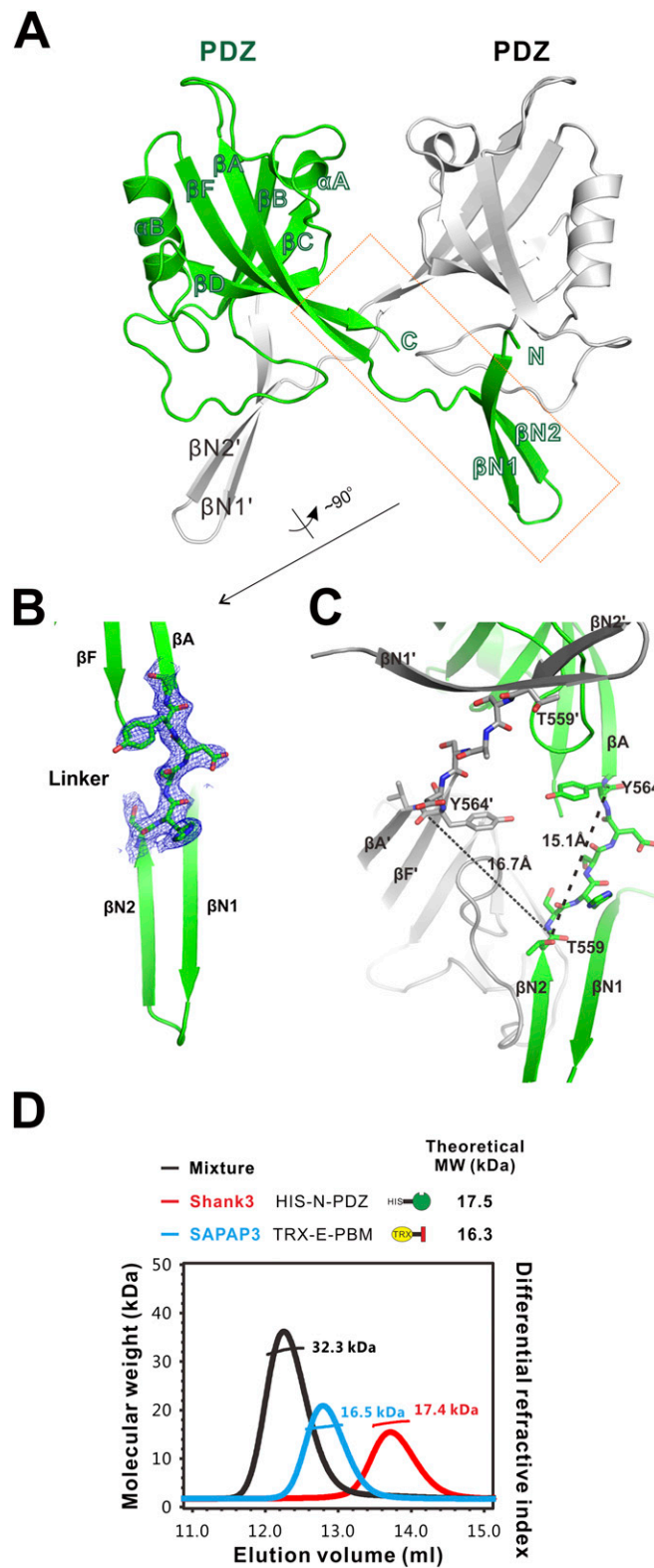
Fig. S1. Shank3 N-PDZ is a monomer in solution with or without SAPAP3 E-PBM binding. (*A*) Ribbon representation of the Shank3 N-PDZ swapped dimer observed in the crystal of the Shank3 N-PDZ/SAPAP3 E-PBM complex. One molecule is shown in green, and the other is in silver. The SAPAP3 peptide is omitted. (*B*) A 2*Fo-Fc* map of the linker residues between the N-extension and PDZ showing that the densities of all residues are continuous and can be clearly assigned. The map is calculated from the final PDB file and contoured at 1.0 σ. (*C*) The distances between the carboxyl carbon of the first residue (T559) of the linker to that of the last residue (Y564) of the linker residues from the same molecule or from the neighboring molecule are very similar (15.1 Å vs. 16.7 Å). This analysis indicates that Shank3 N-PDZ should be stable without forming a domain-swapped dimer. (*D*) Analytical gel filtration chromatography analysis coupled with static light scattering analysis of Shank3 N-PDZ (red line), SAPAP3 E-PBM (blue line), and the Shank3 N-PDZ/SAPAP3 E-PBM complex (black line). Measured molecular weights are labeled in the figure. The theoretical molecular weights of Shank3 N-PDZ and SAPAP3 E-PBM are listed above the graph. The data indicate that Shank3 N-PDZ and SAPAP3 E-PBM form a stable 1:1 complex in solution.
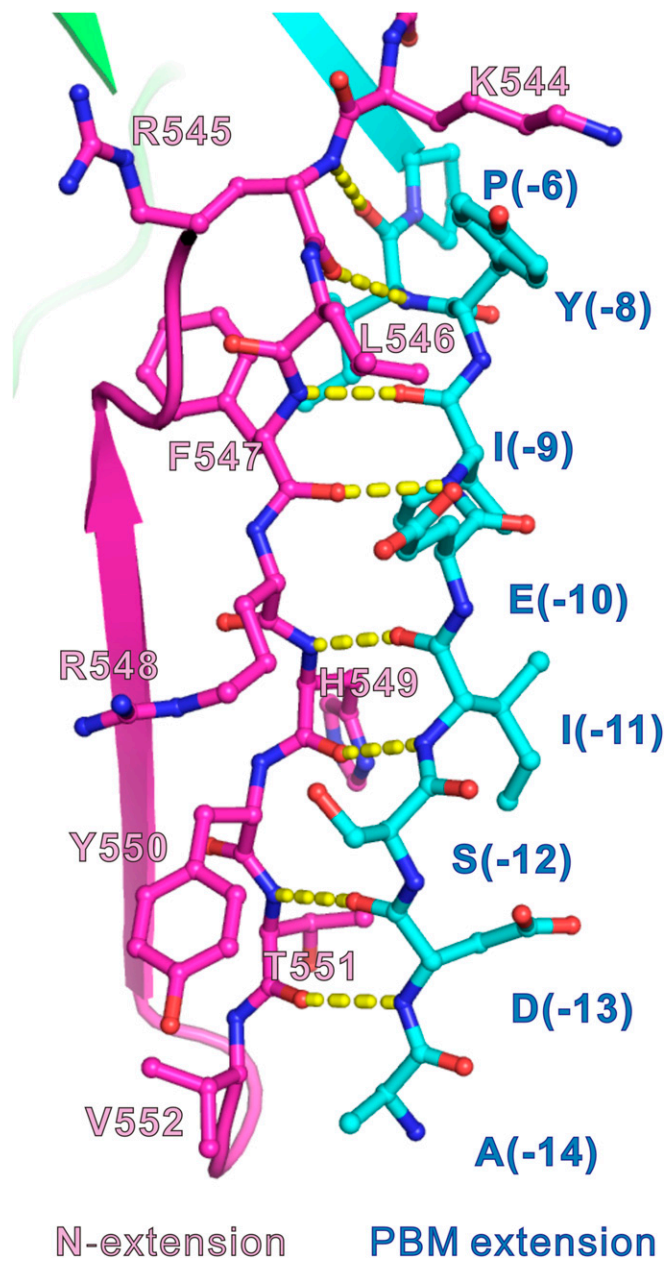
Fig. S2. Structure of the β-strand pairing between the SAPAP3 extended PBM (cyan) and the Shank3 PDZ N-extension (magenta).

Fig. S3. Structure comparisons of the binding mode of the PBM region between the Shank3 N-PDZ/SAPAP3 E-PBM complex (*A*) and the Shank1 PDZ/SAPAP PBM complex (*B*).

Fig. S4. Comparison of the structures of Shank PDZ domain observed in the N-PDZ/SAPAP3 E-PBM complex and in other previously solved structures. (*A*) Overlay of the PDZ domain structures from the N-PDZ/SAPAP3 E-PBM complex of this work, the Shank1 PDZ/SAPAP PBM complex (PDB ID code 1Q3P; white-gray), apo-form PDZ (PDB ID code 1Q3O; violet), and Shank1 PDZ/β-PIX complex (PDB ID code 3L4F; marine). The main difference in these structures is in the BC loop region. (*B*) Close-up view of the BC loop region. (*C*) In the Shank3 N-PDZ/SAPAP3 E-PBM complex, a number of hydrophobic residues in the BC loop interact with one another, forming a large hydrophobic surface (Fig. 2 *D* and *E*). (*D–F*) In other PDZ structures, the electron densities of the BC loops are not well defined. Accordingly, the hydrophobic pocket observed in the N-PDZ/SAPAP3 E-PBM complex is not properly formed, as indicated by the residues colored in red. In *C–F*, backbones of BC loops are rendered as Putty mode in PyMOL; the higher the B-factors, the wider the radius of the backbone sausages.

Fig. S5. Validation of the specific Shank3/SAPAP3 interaction mediated by the N-PDZ/E-PBM complex. (*A*) Co-IP assay comparing interactions between the full-length WT Shank3 and the full-length SAPAP3 or its E-PBM mutants. (*B*) GST pull-down assay comparing interactions between Shank3 SH3-PDZ and the full-length SAPAP3 WT or its E-PBM mutants. (*C*) GST pull-down assay comparing interactions between the SAPAP3 C terminus and the full-length GFP-Shank3 WT or its N-PDZ mutants. Actin was immunoblotted as an input loading control, suggesting that all four Shank3 constructs were expressed at comparable levels in heterologous cells.

Table S1. Statistics for X-ray crystallographic data collection and model refinement

Statistic	Value
Data collection	
Source	SSRF-BL17U
Space group	*P 31 1 2*
Unit cell parameters	
a, b, c (Å)	*a* = 72.824, *b* = 72.824, *c* = 116.360
α, β, γ, °	α = 90.00, β = 90.00, γ = 120.00
Resolution range, Å	50.00–2.50 (2.54–2.50)
No. of unique reflections	12,561 (608)
Redundancy	6.3 (6.5)
$I/\sigma(I)$	35.2 (4.8)
Completeness (%)	99.9 (100.0)
R_{merge} (%)*	6.8 (60.8)
Wilson_B	49.5
Structure refinement	
Resolution, Å	42.7–2.49 (2.75–2.49)
R_{work}[†]/R_{free}[‡] %	18.30 (27.94)/25.06(38.62)
rmsd bonds (Å/angles) °	0.008/1.010
Number of reflections	
Working set	11,914
Test set	610
Number of protein atoms	2,137
Number of water atoms	95
Average B factor ($Å^2$)	
Protein (main chain)	59.3 (61.7)
Water	33.8
Ramachandran plot (%)	
Most favored regions	98.1
Additionally allowed	1.9
Generously allowed	0

Numbers in parentheses represent the value for the highest-resolution shell.

*$R_{merge} = \sum |I_i - I_m| / \sum I_i$, where I_i is the intensity of the measured reflection and I_m is the mean intensity of all symmetry- related reflections.

[†]$R_{cryst} = \Sigma ||F_{obs}| - |F_{calc}|| / \Sigma |F_{obs}|$, where F_{obs} and F_{calc} are the observed and calculated structure factors.

[‡]$R_{free} = \Sigma_T ||F_{obs}| - |F_{calc}|| / \Sigma_T |F_{obs}|$, where T is a test dataset of ∼5% of the total reflections chosen randomly and set aside before refinement.